Structural Response Sensitivity to Rupture Parameter Variations: A High-Fidelity Analysis of a 10-Story Building on the San Ramón Fault

P. Palacios [(1)], M.B. Nicolas [(2)], A. José [(3)]
(1) Universidad de los Andes, Chile, pxpalacios@miuandes.cl
(2) Universidad de los Andes, Chile, nmora@miuandes.cl
(3) Universidad de los Andes, Chile, jaabell@miuandes.cl

ABSTRACT

This paper quantifies the sensitivity of structural response to stochastic rupture variability for near-fault scenarios on the San Ramón Fault, Santiago, Chile. Stochastic finite-fault ground motions for Mw 6.5 and Mw 6.6, with three realizations each, are applied to a linear elastic 10-story reinforced concrete building via the Domain Reduction Method at three site locations spanning 3.3 to 22.5 km from the fault. A three-factor ANOVA at each floor level disaggregates total response variance into contributions from moment magnitude, stochastic slip distribution, and source-to-site distance. Source-to-site distance dominates, explaining 60% to 95% of variance, while stochastic rupture variability contributes 5% to 20%. Inter-realization displacement differences exceed 100% at the nearest station, indicating that a single deterministic scenario is insufficient to characterize near-fault structural demand.

1 INTRODUCTION

The San Ramón Fault is a west-verging reverse fault located at the eastern foothills of Santiago, Chile, capable of generating earthquakes up to Mw 7.0 (Armijo et al., 2010; Gallardo et al., 2025) (Valdés et al., 2025)representing one of the most significant seismic threats to the metropolitan area. Its proximity to densely populated urban districts, with surface rupture projections extending beneath the city, makes it a critical case study for near-fault performance-based earthquake engineering.

Stochastic finite-fault simulations (Liu et al., 2006 ; Schmedes et al., 2010) are widely used to generate physically consistent ground motion ensembles that share magnitude and fault geometry but differ in slip distribution, rise time, and rupture velocity. These ensembles capture the epistemic uncertainty inherent in the rupture process and provide a natural framework for sensitivity analysis. However, most existing studies examine ground motion variability at the free surface or at reference rock conditions, without propagating this uncertainty through the complete source-to-structure chain. The extent to which stochastic rupture variability influences engineering demand parameters at the structural level, particularly when soil-structure interaction is explicitly modeled, remains poorly characterized for near-fault urban scenarios.

This paper addresses this gap by quantifying the sensitivity of structural response to stochastic rupture variability for scenarios on the San Ramón Fault. Ground motions are computed using the frequency-wavenumber (FK) method (Bouchon & Aki, 1977; Zhu & Rivera, 2002) implemented in ShakerMaker (Abell et al., 2022) and applied to a linear elastic 10-story reinforced concrete building via the Domain Reduction Method (Bielak, 2003; Yoshimura et al., 2003) in OpenSees (McKenna et al., 2010).

2 METHODOLOGY

Figure 1 presents the geographical configuration of the three DRM stations selected for analysis and the reference coordinate system used throughout the study. Station **sta_3** is located at 3.3 km, **sta_6** at 10.4 km and **sta_9** at 22.5 km measured from the western edge of the fault projection. The coordinate system is oriented such that the longitudinal axis of the building is parallel to the X component and the transverse axis is parallel to the Y component. This distance range spans near-fault to intermediate-field conditions, covering a broad spectrum of urban exposure in Santiago.

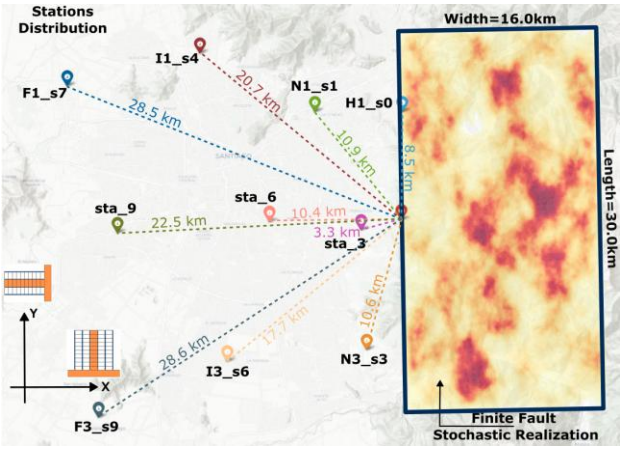


Figure 1. Geographical distribution of station locations relative to the San Ramón Fault plane.

2.1 Seismic Source & Stochastic Realizations

Seismic sources are generated using the Finite-Fault Stochastic Generator with Double Corner Frequency, which produces spatially correlated distributions of kinematic rupture parameters including slip amplitude, rise time, and rupture velocity, constrained by seismological

observations (Wells & Coppersmith, 1994; Liu et al., 2006; Schmedes et al., 2010). Two moment magnitudes are considered: Mw 6.5 and Mw 6.6, with three realizations per magnitude, capturing the epistemic uncertainty associated with the rupture process. Figure 2 presents the finite-fault slip distributions for all stochastic realizations considered in this study. The upper row corresponds to Mw 6.5 and the lower row to Mw 6.6, each showing three realizations (**rup_bl_1**, **rup_bl_2**, and **rup_bl_3**) that share the same fault geometry but differ in slip distribution.

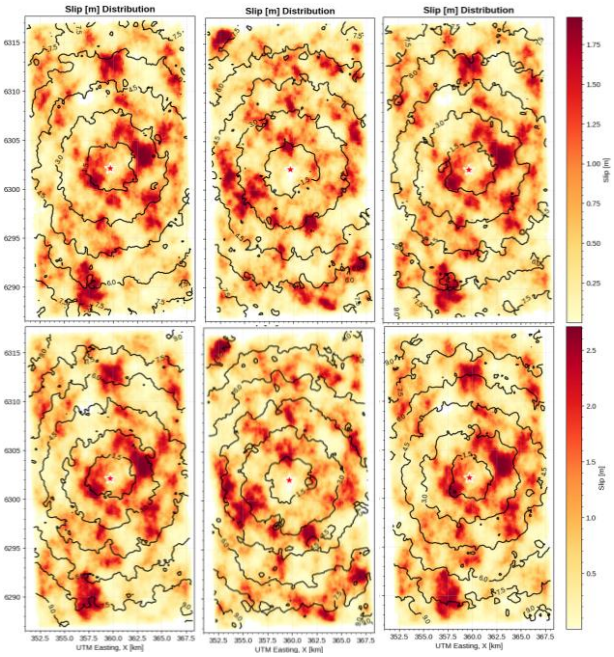


Figure 2. Finite-fault slip distributions for all stochastic realizations considered.

2.2 Wave Propagation — Frequency-Wavenumber Method

Regional-scale seismic wave propagation is computed using the frequency-wavenumber (FK) method (Bouchon & Aki, 1977 ; Zhu & Rivera, 2002) implemented in ShakerMaker (Abell et al., 2022) which assumes a flat, horizontally layered and elastic crust model. The crustal structure is represented as a four-layer stratified medium as shown in Table 1 (Taked from Valdés et al., 2025)

Table 1. Stratified crustal model parameters

Layer	Thickness (km)	Vp (km/s)	Vs (km/s)	ρ (gr/cm3)	Qp	Qs
1	0.20	1.32	0.75	2.40	1000.0	1000.0
2	0.80	2.75	1.57	2.50	1000.0	1000.0
3	14.5	5.50	3.14	2.50	1000.0	1000.0
4	∞	7.00	4.00	2.67	1000.0	1000.0

2.3 High-Fidelity SSI — DRM Configuration

Soil-structure interaction is incorporated via the DRM (Bielak, 2003) (Yoshimura et al., 2003) The reference model consists of a soil box of 100 x 100 x 30 m with Δx = 2.5 m and Δt = 0.0025 s, satisfying both the wave resolution requirement (N = 10 points per wavelength at fmax = 25 Hz) and the CFL stability condition (Courant et al., 1928). Absorbing boundary conditions are implemented through an exterior soil layer surrounding the interior domain, modeled using Rayleigh damping $\mathrm{C} = \alpha_M M + \beta_K K$, calculated at f1 =1Hz and f2 =10 Hz with a target damping ratio $\xi = 0.02$

2.4 Structural Model

Figure 3 shows the structural model and represents a typical 10-story reinforced concrete building common in Chile, modeled in STKO (Petracca & Camata, 2021) and developed in OpenSees (McKenna et al., 2010). with linear elastic behavior. The building uses normal-strength concrete (fc = 28 MPa, Ec = 25000 MPa), with columns (0.70 x 0.70 m), solid slabs (0.20 m), shear wall (0.30m) and a foundation slab (0.70 m).

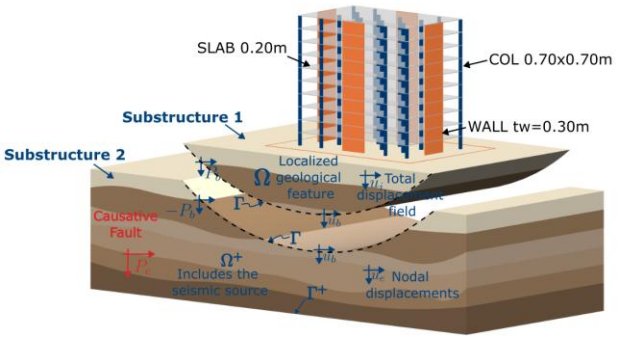


Figure 3. DRM model idealization for the ten-story reinforced concrete building

The DRM framework decomposes the problem into two substructures: an exterior domain (Substructure 2) that includes the causative fault and the regional wave propagation and an interior localized domain (Substructure 1) that contains the soil-structure system of interest. Equivalent nodal forces computed at the DRM boundary layer couple both substructures, transferring the incoming wavefield into the localized model without spurious reflections.

3 RESULTS & DISCUSSION

3.1 Ground Motion Variability at Foundation Level

Ground motion characteristics at the foundation level (z = 0) are examined through power spectral density (PSD) analysis and Arias Intensity (IA) across the three DRM stations and two moment magnitudes considered. Figure 4 presents the mean Fourier PSD for components X and Y at each station for Mw 6.5 and Mw 6.6.

The Fourier PSD analysis reveals a distance-dependent amplitude decay across the full frequency range, with sta_3 consistently exhibiting the highest power at all frequencies. This attenuation is frequency-dependent: at low frequencies (below 25 Hz) the three stations show relatively similar spectral amplitudes, while moderate

differences emerge in the 25-50 Hz band and significant separation is observed above 50 Hz. This behavior is consistent with frequency-dependent anelastic attenuation, which selectively dissipates high-frequency energy over propagation distance. The spectral shape is largely preserved across stations, reflecting the fact that the stratified crustal model remains unchanged between scenarios. Minor shape variations between magnitudes are nonetheless expected given the different corner frequencies associated with Mw 6.5 and Mw 6.6.

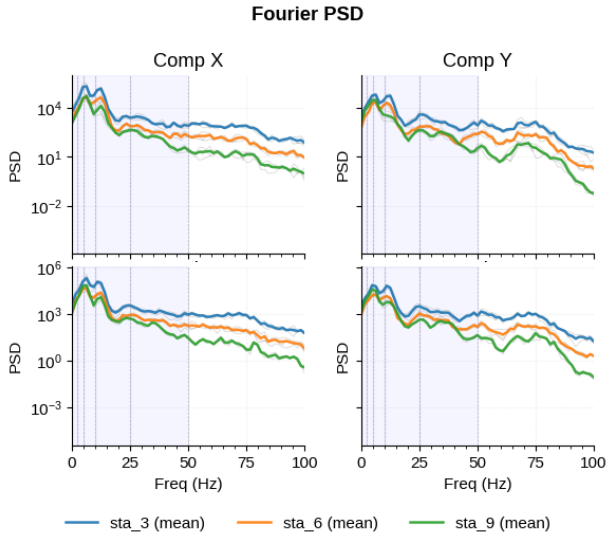


Figure 4. Mean Fourier PSD at foundation level (z = 0) for Mw 6.5 and Mw 6.6.

This distance-dependent attenuation is further confirmed by the Arias Intensity results shown in Figure 5. For the mean realization, sta_3 yields IA values of 6.84 m/s and 2.96 m/s for components X and Y respectively, compared to 1.74 m/s and 0.88 m/s for sta_6, and 1.37 m/s and 0.90 m/s for sta_9. The inter-station ratio reaches approximately 5:1 in the X component, indicating that source-to-site distance is the dominant factor governing ground motion intensity at the foundation level for the configuration studied.

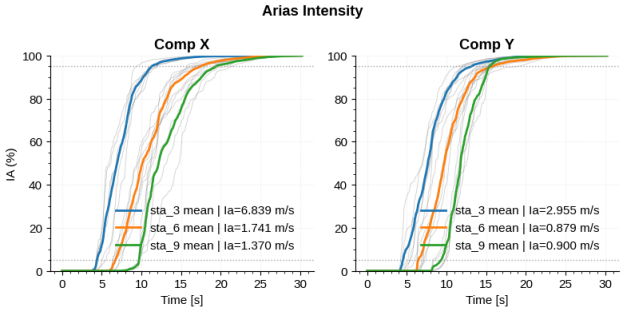


Figure 5. Arias Intensity cumulative curves at foundation level (z = 0) mean realization per station.

Figure 6 complements this analysis by presenting the PGA values disaggregated by rupture realization and station for both moment magnitudes considered, with each column corresponding to a different magnitude (Mw 6.5 and Mw 6.6). Station sta_3 consistently exhibits the highest PGA values across all realizations and magnitudes, confirming the distance-dependent attenuation previously observed. Notably, the stochastic nature of the rupture process introduces non-negligible variability among realizations sharing the same magnitude: individual seeds produce distinct slip distributions that result in different excitation levels at each station. This inter-realization scatter is particularly evident at sta_3, where proximity to the fault amplifies the sensitivity to source variability, while sta_6 and sta_9 show more homogeneous responses across realizations due to geometric attenuation effects.

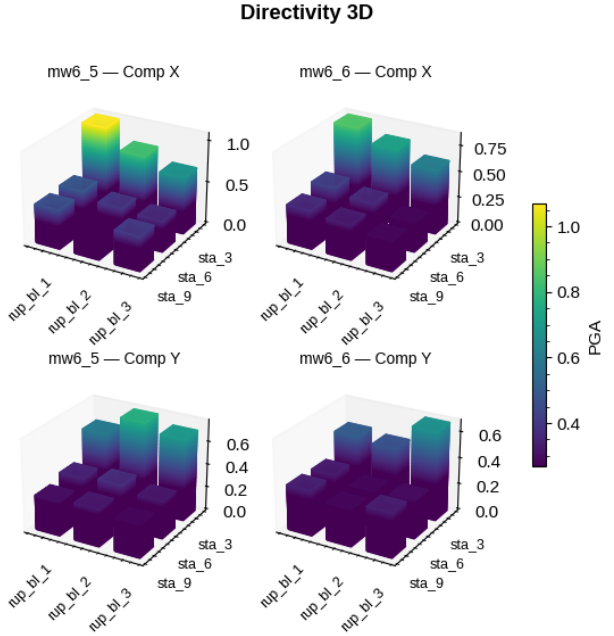


Figure 6. PGA per rupture realization, DRM station, and moment magnitude.

3.2 Floor-Level Structural Response

The displacement orbits at the roof level (z = 35.0 m) are presented in Figure 7 for both moment magnitudes and all rupture realizations. Each orbit represents the relative displacement trajectory between the roof and the foundation in the horizontal plane, providing a direct measure of the building's bidirectional demand envelope.

Three key observations emerge from this analysis. **First**, the orbit amplitude is strongly governed by source-to-site distance, with sta_3 exhibiting significantly larger displacements than sta_6 and sta_9 across all realizations and magnitude. For Mw 6.6, the maximum resultant displacement at sta_3 reaches 268.5 mm, compared to 116.2 mm and 71.4 mm at sta_6 and sta_9 respectively. **Second**, stochastic rupture variability introduces substantial scatter in the near-fault response. At sta_3, the maximum resultant displacement varies from 123.9 mm (rup_bl_3) to 268.5 mm (rup_bl_1) for Mw 6.6, representing a difference exceeding 100% between realizations sharing the same magnitude and fault geometry but differing only in slip distribution. This highlights that a single deterministic rupture scenario may significantly underestimate or overestimate structural demand depending on the realization selected, underscoring the necessity of

ensemble-based approaches in near-fault performance assessment. **Third**, the shape and orientation of the displacement orbits vary across realizations, indicating that stochastic slip distribution not only scales the response amplitude but also modifies its bidirectional character. Different seeds produce distinct preferential displacement directions, which have direct implications for the assessment of torsional demands and directionality effects in structural design. At sta_9, orbits are compact and consistent across realizations, suggesting that geometric attenuation reduces both the intensity and the inter-realization variability of the structural demand at greater distances from the fault.

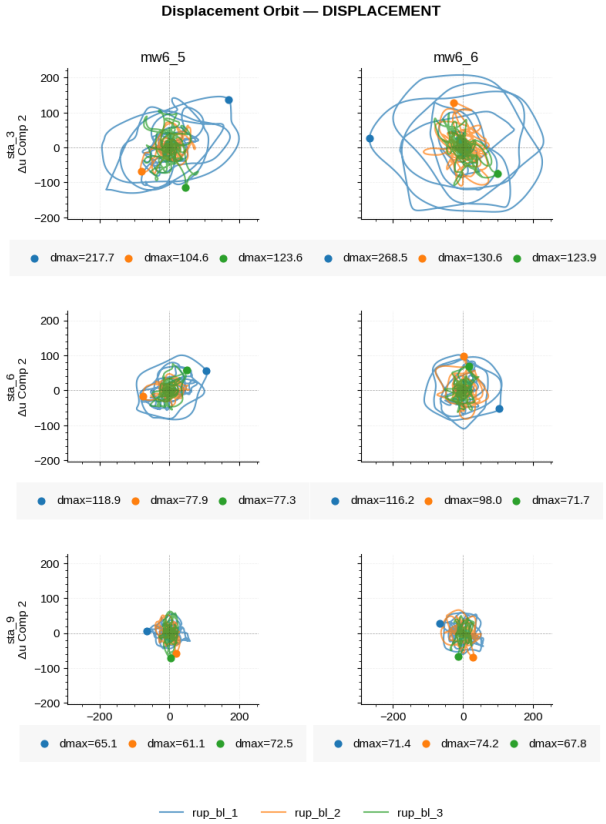


Figure 7. Displacement orbits at roof level for all rupture realizations and moment magnitudes across DRM stations.

3.3 EDP Sensitivity & Inter-Realization Variability

To quantify the relative contribution of each source of variability to the structural response, a three-factor Analysis of Variance (ANOVA) was performed at each floor level. The additive model adopted takes the form equation 1.

$$y_ijk = \mu + \alpha_i + \beta_j + \gamma_k + \varepsilon_ijk \quad [1]$$

where y_ijk denotes the engineering demand parameter (EDP) evaluated at a given floor level, μ is the overall mean, α_i represents the effect of moment magnitude (Mw 6.5 and Mw 6.6), β_j the effect of stochastic rupture realization (rup_bl_1, rup_bl_2, rup_bl_3), γ_k the effect of DRM station (sta_3, sta_6, sta_9), and ε_ijk the residual error. Prior to ANOVA, a logarithmic transformation was applied to all EDP values to stabilize variance across stations. Formal assumption testing using Shapiro-Wilk and Levene tests confirmed that normality and homoscedasticity hold at all floor levels after transformation, with isolated exceptions at z = 31.5 m in component X, likely associated with modal amplification effects near the roof level. The model assumes factor additivity, residual normality, and homoscedasticity. The design is fully balanced, with identical factor combinations across both magnitudes, yielding 18 observations per floor level and 12 residual degrees of freedom. The proportion of total variance explained by each factor is quantified through the eta-squared index η^2 = SS_factor / SS_total, where SS denotes the sum of squares.

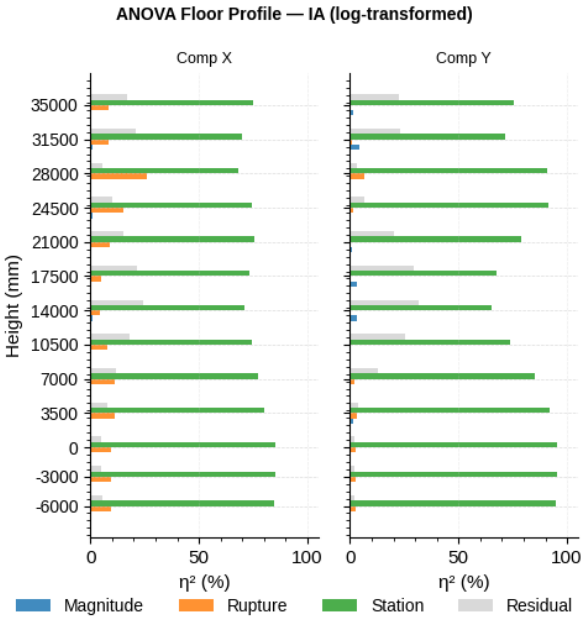


Figure 8. ANOVA floor profile of eta-squared (η^2) for Arias Intensity across all floor levels.

Figure 8 presents the η^2 floor profiles for components X and Y for Arias Intensity. The results reveal a clear hierarchy of influence across all floor levels and both components. The DRM station, which serves as a proxy for source-to-site distance, is the dominant factor, explaining between 60% and 95% of the total variance. This confirms that geometric attenuation governs the ground motion intensity reaching the structure, as already observed in the foundation-level analysis. The stochastic rupture realization contributes a secondary but consistent effect, accounting for approximately 5% to 20% of the variance depending on the floor level, demonstrating that slip variability propagates through the full source-to-structure chain and produces non-negligible differences in structural demand. Moment magnitude, given the narrow range considered (ΔMw = 0.1), contributes less than 5% of the variance at all floors. The residual fraction is generally low, indicating that the additive model provides an adequate representation of the variance structure for the scenario ensemble studied. A slight increase in the rupture effect is observed at lower floor levels relative to upper floors, suggesting that the

foundation input motion retains greater sensitivity to source variability than the amplified response at higher elevations, where modal filtering by the structure tends to reduce inter-realization differences.

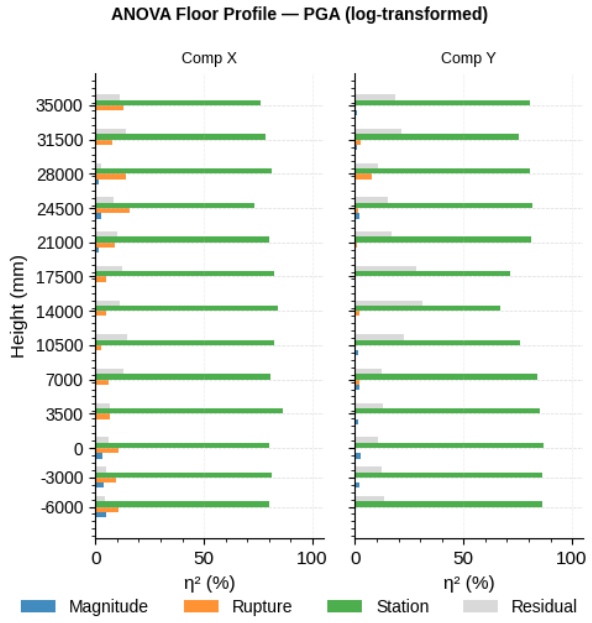


Figure 9. ANOVA floor profile of eta-squared (η²) for PGA across all floor levels.

Figure 9 presents the η² floor profiles for PGA across components X and Y. The station factor remains dominant across all floor levels, consistent with the Arias Intensity results. However, several additional observations emerge from this analysis.

The rupture realization contributes more to component X than to component Y across all floor levels. Given the fault orientation and the coordinate system defined in Figure 1, component X receives ground motion energy more directly aligned with the rupture propagation direction, making the structural demand in this component more sensitive to slip distribution variability. Component Y, being more oblique to the wave propagation direction, is dominated almost entirely by the station factor, with rupture contributing a smaller and more uniform effect across all floors.

A height-dependent pattern is also observed. At subterranean levels (z = -3.00 and -6.00 m), the rupture effect carries greater relative weight compared to floors above grade, suggesting that the embedded portion of the structure responds differently to source variability than the superstructure. At upper floors, the residual fraction increases slightly for component X, indicating that modal amplification introduces additional variability not fully captured by the additive model.
Moment magnitude contributes less than 5% of the variance at all floors and both components, confirming that the narrow magnitude range considered does not produce statistically distinguishable differences in peak floor acceleration.

3.4 Limitations

Several limitations of the present study should be acknowledged. The structural model assumes linear elastic behavior throughout, which is appropriate for a first characterization of the source-to-structure sensitivity but does not capture the inelastic demand redistribution that would occur in a realistic near-fault scenario with the displacement amplitudes observed at sta_3. Additionally, the ensemble size of three realizations per magnitude, while sufficient to identify dominant trends, limits the statistical power of ANOVA and prevents robust estimation of higher-order interaction effects between factors. Results should therefore be interpreted as indicative rather than exhaustive characterizations of the rupture parameter space.

4 CONCLUSIONS

This study investigated the sensitivity of structural response of a linear elastic 10-story reinforced concrete building to stochastic rupture variability for near-fault earthquake scenarios on the San Ramón Fault, Santiago, Chile. A three-factor ANOVA framework was applied at each floor level to disaggregate total response variance into contributions from moment magnitude, stochastic slip distribution, and source-to-site distance. The following conclusions are drawn from the analysis.

Source-to-site distance is the dominant factor governing structural demand across all floor levels and both horizontal components, explaining between 60% and 95% of total response variance. This confirms that geometric attenuation controls ground motion intensity in the near-fault to intermediate-field distance range studied, and that site location is the primary variable to consider in performance-based assessments for structures near the San Ramón Fault.

Stochastic rupture variability produces a secondary but physically meaningful contribution of 5% to 20% of total variance, demonstrating that slip distribution uncertainty propagates through the complete source-to-structure chain. At the nearest station, inter-realization displacement differences exceed 100% (See Figure 7), underscoring that a single deterministic scenario is insufficient to characterize near-fault structural demand and that ensemble-based approaches are necessary.

Displacement orbit analysis reveals that stochastic slip distribution modifies not only the amplitude but also the directionality of the structural response. Different rupture realizations produce distinct preferential displacement directions at the roof level, with direct implications for torsional demand assessment and directionality effects in structural design.

A directional dependence of rupture sensitivity is identified. Component X, aligned with the longitudinal axis of the building and more directly exposed to the rupture propagation direction, exhibits greater sensitivity to stochastic slip variability than component Y. This finding

has direct implications for directionality considerations in structural design and ground motion selection for near-fault sites.

Moment magnitude, over the narrow range of Mw 6.5 to Mw 6.6 considered, contributes less than 5% of total variance at all floors. Its primary effect is the scaling of ground motion amplitude without significant modification of spectral shape, as confirmed by the Fourier PSD analysis.

These results support the adoption of ensemble-based ground motion approaches for performance-based earthquake engineering assessments of structures located in near-fault environments, where rupture stochasticity represents a non-negligible source of epistemic uncertainty that cannot be captured by deterministic scenario analyses.

Future work will extend this analysis to nonlinear structural models, a broader ensemble of rupture realizations, and additional rupture idealization scenarios including unilateral propagation, to more comprehensively characterize the epistemic uncertainty associated with the rupture process on the San Ramón Fault.

5 ACKNOWLEDGMENTS

The authors acknowledge the support from the Chilean National Research and Development Agency (ANID), FONDECYT Iniciación project No. 11220530. The scholarship programs of Becas ANID of the Chilean government and FAI of Universidad de los Andes are also acknowledged.

6 REFERENCES

Abell, J. A., Crempien, J. G. F., & Recabarren, M. (2022). ShakerMaker: A framework that simplifies the simulation of seismic ground-motions. *SoftwareX*, *17*, 100911. https://doi.org/10.1016/j.softx.2021.100911

Armijo, R., Rauld, R., Thiele, R., Vargas, G., Campos, J., Lacassin, R., & Kausel, E. (2010). The West Andean Thrust, the San Ramón Fault, and the seismic hazard for Santiago, Chile. *Tectonics*, *29*(2), n/a-n/a. https://doi.org/10.1029/2008tc002427

Bielak, J. (2003). Domain Reduction Method for Three-Dimensional Earthquake Modeling in Localized Regions, Part I: Theory. *Bulletin of the Seismological Society of America*, *93*(2), 817–824. https://doi.org/10.1785/0120010251

Bouchon, M., & Aki, K. (1977). Discrete wave-number representation of seismic-source wave fields. *Bulletin of the Seismological Society of America*, *67*(2), 259–277. https://doi.org/10.1785/BSSA0670020259

Courant, R., Friedrichs, K., & Lewy, H. (1928). Uber die partiellen Differenzengleichungen der mathematischen Physik. *Mathematische Annalen*, *100*(1), 32–74. https://doi.org/10.1007/BF01448839

Gallardo, J., Chacón, M., Muñoz, J., Gutiérrez-Urzúa, F., Cembrano, J., Rossetto, T., Freddi, F., Crempien, J., & de la Llera, J. C. (2025). Earthquake response sensitivity of HDRB Base-Isolated Hospitalsto the Crustal San Ramón Fault in Santiago, Chile. *Under Review*, 1–24. https://doi.org/10.1002/eqe.70154

Liu, P., Archuleta, R. J., & Hartzell, S. H. (2006). Prediction of broadband ground-motion time histories: Hybrid low/high-frequency method with correlated random source parameters. *Bulletin of the Seismological Society of America*, *96*(6), 2118–2130. https://doi.org/10.1785/0120060036

McKenna, F., Scott, M. H., & Fenves, G. L. (2010). Nonlinear Finite-Element Analysis Software Architecture Using Object Composition. *Journal of Computing in Civil Engineering*, *24*(1), 95–107. https://doi.org/10.1061/(asce)cp.1943-5487.0000002

Petracca, M., & Camata, G. (2021). *STKO User Manual*. ASDEA Software Technology.

Schmedes, J., Archuleta, R. J., & Lavallée, D. (2010). Correlation of earthquake source parameters inferred from dynamic rupture simulations. *Journal of Geophysical Research: Solid Earth*, *115*(3), 1–12. https://doi.org/10.1029/2009JB006689

Valdés, A. H., Torres, E., Camata, G., Petracca, M., Crempien, J. G. F., & Abell, J. A. (2025). Impact of Soil–Structure Interaction Modeling Simplifications and Structural Nonlinearity on Uncertainty in EDPs: A Case Study on an Existing RC Building in Santiago. *Earthquake Engineering and Structural Dynamics*, *54*(8), 2062–2083. https://doi.org/10.1002/eqe.4340

Wells, D. L., & Coppersmith, K. J. (1994). New empirical relationships among magnitude, rupture length, rupture width, rupture area, and surface displacement. *Bulletin - Seismological Society of America*, *84*(4), 974–1002. https://doi.org/10.1785/bssa0840040974

Yoshimura, C., Bielak, J., Hisada, Y., & Fernández, A. (2003). Domain reduction method for three-dimensional earthquake modeling in localized regions, part II: Verification and applications. *Bulletin of the Seismological Society of America*, *93*(2), 825–840. https://doi.org/10.1785/0120010252

Zhu, L., & Rivera, L. A. (2002). A note on the dynamic and static displacements from a point source in multilayered media. *Geophysical Journal International*, *148*(3), 619–627. https://doi.org/10.1046/j.1365-246X.2002.01610.x